https://doi.org/10.31891/csit-2026-2-14

Eugene FEDOROV
Dr. Sc. in Technical Sciences, Professor,
Professor of Department of Statistics and Applied Mathematics
Cherkasy State Technological University
https://orcid.org/0000-0003-3841-7373
y.fedorov@chdtu.edu.ua

Tetyana UTKINA
Ph. D. in Technical Sciences, Associate Professor, Associate Professor of Department of Robotics and Specialized Computer Systems
Cherkasy State Technological University
https://orcid.org/0000-0002-6614-4133
t.utkina@chdtu.edu.ua

Yaroslav KORPAN
Ph. D. in Technical Sciences, Associate Professor, Associate Professor of Department of Robotics and Specialized Computer Systems
Cherkasy State Technological University
https://orcid.org/0000-0002-1455-5977
y.korpan@chdtu.edu.ua

Received: 16/04/2026
Accepted: 12/05/2026
Published: 31/05/2026

UDC 004.89

METHODS FOR DIAGNOSIS OF MELANOMA BASED ON DIGITAL IMAGE PROCESSING AND EXPERT SYSTEMS

This article proposes a solution to a pressing scientific and applied problem: the development of a method for diagnosing melanoma based on a fuzzy expert system and digital image processing. The method for calculating melanoma features based on digital image processing proposed in the article includes: conversion of a color image into a grayscale image; conversion of a grayscale image into a binary image based on single-level global thresholding using the Otsu threshold; removal of small objects from the binary image using morphological transformation; formation of a binary matrix of image point membership to the object and a grayscale image of the object; determination of the object boundary in the binary image after morphological transformation based on the Kanna method; calculation of the irregularity of the object boundary in the binary image after morphological transformation; determination of the number of colors based on clustering of the gray-scale image object; rotation of the gray-scale image object; calculation of the diameter of the rotated gray-scale image object; verification of asymmetry based on the rotated gray-scale image object. For the diagnosis of melanoma, this work improved a fuzzy expert system for melanoma diagnosis that uses Sugeno's fuzzy inference algorithm. An experimental study confirmed that the proposed fuzzy expert system achieves a probability of incorrect decisions regarding melanoma diagnosis of 0.02 and a root mean square error of 0.05. The scientific novelty of the study lies in the fact that the proposed fuzzy expert system represents knowledge about melanoma in the form of fuzzy rules that are understandable to humans; it reduces computational complexity, the probability of making an incorrect decision, and the root mean square error. The proposed solution is scalable and suitable for use in intelligent decision-making systems.

Keywords: fuzzy expert system for melanoma diagnosis, image binarization, geometric image transformations, image clustering, object boundary detection, morphological image transformations.

Introduction

In the 21st century, skin melanoma remains one of the most dangerous malignant tumors, and its incidence is steadily rising, despite declining rates for many other types of cancer. This negative trend has been particularly pronounced over the past 40 years among the Caucasian population. A striking example is provided by statistics from the United States, where melanoma ranks fifth and sixth among all cancers in men and women, respectively, and the incidence rate increased by 270% between 1973 and 2002. According to current data, the lifetime risk of developing melanoma in developed countries reaches 2% [1, 2].

According to data from the IARC (GLOBOCAN) 2022 data (Fig. 1 [3]), melanoma ranks 17th in the global cancer incidence pattern: more than 331,000 new cases and approximately 58,000 deaths are reported annually [4, 5].

An analysis of the interactive map on skin melanoma (Fig. 1 [3]) able to reveals three key patterns [4-6]:

1. Phenotype and Sun Exposure (The Oceania Paradox). Australia and New Zealand are colored the darkest (index 37.0). A combination of high levels of ultraviolet (UV) radiation and a population with fair skin (phototypes I-II) that is genetically unprotected from such sunlight. This is the absolute global maximum.
2. The "North–South" gradient in Europe. In Europe, the opposite relationship is observed: the further north a country is, the higher the incidence. In Scandinavia (Denmark, Norway, Sweden) rates are among the highest in the world (around 30.0). In Mediterranean (Italy, Greece) rates are

significantly lower (around 10.0-12.0), despite abundant sunshine. The light sensitivity of northerners' skin plays a greater role than simply the number of sunny days.

3. Economic Factors and Reporting. The map shows low incidence rates in Africa and Asia (less than 1.0). This is due to biological protection, since high melanin content in the skin provides effective protection against melanoma. Another factor is statistical barrier, since in a number of developing countries, low figures may be due to underdiagnosis and the lack of high-quality cancer registries.

4. The global age-standardized incidence rate is 3.20 per 100,000 population; however, the epidemiological picture is highly heterogeneous and varies significantly depending on the region and the populations phototype. The highest incidence rates (as measured by the age-standardized rate per 100,000 population) are observed in Oceania, North America, and Europe (Fig. 2).

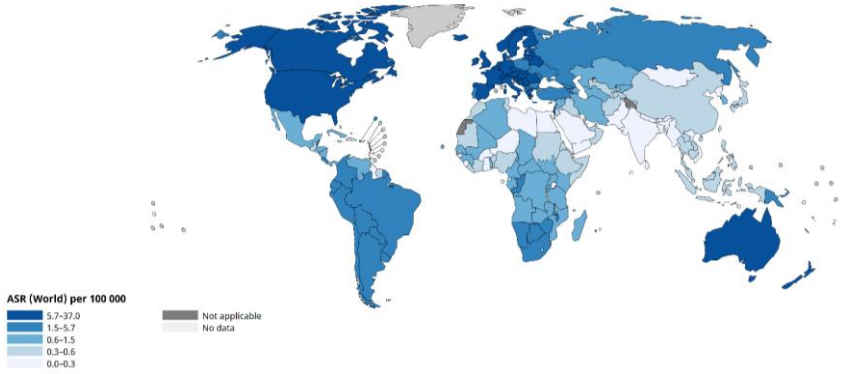

Fig. 1 The incidence of skin melanoma (age-standardized rate per 100,000 population) worldwide

The etiopathogenesis of melanoma is multifactorial and determined by the complex interaction of exogenous and endogenous factors. Exposure to ultraviolet (UV) radiation remains a key modifiable risk factor. Studies confirm that periodic sun exposure and a history of sunburn more than double the relative risk of developing the tumor.

Significant internal predictors include:

1. Phenotypic characteristics: fair skin phototypes (Fitzpatrick I-II), presence of more than 100 common or multiple atypical nevi.

2. Genetic predisposition: germline mutations in tumor suppressor genes, such as CDKN2A and CDK4, as well as polymorphisms in the MC1R gene, which is responsible for pigmentation.

3. Family history: family cases of melanoma (identified in 5–14% of cases) and immunosuppressive conditions significantly increase the lifetime risk of developing the disease.

4. The high level of somatic mutations caused by cumulative UV exposure explains the marked genetic heterogeneity of melanoma, which requires in-depth study of its molecular profile to improve strategies for early diagnosis and targeted therapy.

The high rate of somatic mutations caused by prolonged exposure to ultraviolet radiation explains the marked genetic heterogeneity of melanoma, underscoring the need for in-depth study of its molecular profile to improve strategies for early diagnosis and targeted therapy.

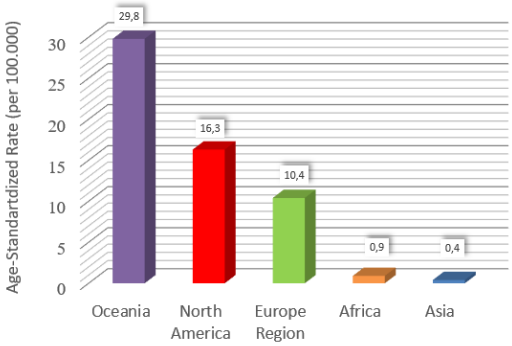

Fig. 2 Incidence of skin melanoma among the white population (age-standardized rate per 100,000 population)

A key factor determining the need to improve existing methods for diagnosing melanoma is the stage-dependent nature of the prognosis [7].

Once distant metastases are detected, the survival rate drops sharply to 27–30% [3, 4].

In the early stages, the high variability of morphological features often leads to errors in subjective assessment, creating a critical need for automated systems for the preventive diagnosis of melanoma capable of detecting minimal atypical changes that are invisible to the human eye.

In the late stages, the cost of melanoma treatment (immunotherapy, targeted therapy) is tens of times higher than the cost of early surgical intervention, making mass screening a priority for healthcare systems.

According to data from the World Health Organization (WHO) and the IARC (GLOBOCAN), melanoma accounts for only about 1% of all skin cancers, yet it is responsible for more than 70% of deaths related to dermatological oncology [3, 4].

Thus, given the aggressive biological nature of melanoma and the rising incidence of the disease [6, 7], the development and refinement of objective diagnostic methods for melanoma represent a pressing priority. The introduction of such methods into modern clinical oncodermatology will help mitigate the influence of the human factor and facilitate a shift from a strategy of treating complications caused by melanoma to a strategy of its preventive, high-precision diagnosis.

Literature review

Currently, the verification of pigmented skin lesions for the purpose of melanoma screening relies on the use of the following analytical methods and objective assessments (Table 1):

1. The ABCDE criteria [8] (if the total score is < 3, the lesion is benign; if the total score is ≥ 3, it is melanoma):

1.1. Asymmetry – benign lesions are symmetrical in shape and color; malignant lesions are asymmetrical in shape and color. One point is assigned for one or more asymmetries in shape and color along the horizontal and vertical axes.

1.2. Border – benign lesions have smooth and well-defined borders; malignant lesions have irregular (notched) borders (assessed across 8 segments). One point is assigned for an irregular border in one or more segments.

1.3. Color – benign lesions have uniform coloring (brown or pink), while malignant lesions have irregular coloring (various shades of brown, black, red, white, or blue). One point is assigned for the presence of one or more colors corresponding to those of a malignant lesion.

1.4. Diameter – benign lesions have a diameter of 6 mm or less, while malignant lesions have a diameter greater than 6 mm. One point is assigned for a diameter greater than 6 mm.

1.5. Evolution – benign lesions show no changes; malignant lesions exhibit changes in size, shape, or color. One point is assigned for one or more changes.

Table 1

Distinguishing a mole from melanoma according to ABCDE

Sign	Nevi	Melanoma
Asymmetry	 Symmetrical	 Asymmetrical
Border	 Regular edges	 Irregular edges
Color	 Single color	 Multiple colors
Diameter	 Up to 6 mm	 Over 6 mm
Evolution	 Does not change over time	 Changes in size, shape, or color

1. ABCD criteria [9] (TDS (Total Dermatoscopy Score) = (A × 1.3) + (B × 0.1) + (C × 0.5) + (D × 0.5); if TDS < 4.75, the lesion is benign; if 4.8 ≥ TDS ≤ 5.45, the lesion is suspicious; if TDS > 5.45, the lesion is melanoma).

1.1. Asymmetry – benign lesions are symmetrical in shape and color; malignant lesions are asymmetrical in shape and color. 0.5 points are assigned for asymmetry in shape along the horizontal (or vertical) axis and 0.5 points for asymmetry in color along the horizontal (or vertical) axis. Thus, the total A score ranges from 0 to 2.

1.2. Border – benign lesions have a smooth border, while malignant lesions have an irregular (jagged) border (assessed across 8 segments). One point is assigned for an irregular border in a single segment. Thus, the total score B ranges from 0 to 8.

1.3. Color – benign lesions have a single color (brown or pink), while malignant lesions have up to 6 colors (light brown, dark brown, black, red, white, and blue-gray). One point is assigned for each color corresponding to the color of a malignant lesion. Thus, the total C score ranges from 0 to 6.

1.4. Diameter – benign lesions have a diameter of 6 mm or less, while malignant lesions have a diameter greater than 6 mm. One point is assigned for a diameter greater than 6 mm. Thus, the total D score is 0 or 1.

2. The ABCD rule [9] (TDS (Total Dermatoscopy Score) = (A × 1.3) + (B × 0.1) + (C × 0.5) + (D × 0.5); if TDS < 4.75, the lesion is benign; if TDS is between 4.8 and 5.45, the lesion is suspicious; if TDS > 5.45, the lesion is melanoma).

2.1. Asymmetry – benign lesions are symmetrical in shape and color; malignant lesions are asymmetrical in shape and color. 0.5 points are assigned for asymmetry in shape along the horizontal (or vertical) axis and 0.5 points for asymmetry in color along the horizontal (or vertical) axis. Thus, the total A score ranges from 0 to 2.

2.2. Border – benign lesions have a well-defined border, while malignant lesions have an irregular border (assessed across 8 segments). One point is assigned for an irregular border in a single segment. Thus, the total score for B ranges from 0 to 8.

2.3. Color – benign lesions have a single color (brown or pink), while malignant lesions have up to 6 colors (light brown, dark brown, black, red, white, and blue-gray). One point is assigned for each color corresponding to the color of a malignant lesion. Thus, the total C score ranges from 0 to 6.

2.4. Dermoscopic – dermoscopic features. One point is assigned for an atypical pigment network, one point for atypical pigmentation, one point for branching, one point for atypical dots, and one point for atypical globules. Thus, the total B score ranges from 0 to 5.

3. Seven-item checklist [10] (if the total score is <3, the lesion is benign; if the total score is ≥ 3, it is melanoma).

3.1. 2 points are assigned for an atypical pigment network.
3.2. 2 points are assigned for an atypical vascular pattern.
3.3. 2 points are assigned for a white-blue or gray-blue area.
3.4. 1 point is assigned for branching.
3.5. 1 point is assigned for atypical pigmentation.
3.6. 1 point is assigned for atypical dots or globules.

4. Three-criteria checklist (if the total score is < 2, the lesion is benign; if the total score is > 2, the lesion is malignant).

4.1. 1 point is awarded for asymmetry in shape and color.
4.2. 1 point is awarded for an atypical pigment network.
4.3. 1 point is assigned for a white-blue or gray-blue area.

The pigment network is a typical structural feature of pigmented skin lesions (Fig. 3). Two types of pigment networks are distinguished: typical and atypical. A typical pigment network has a regular, honeycomb-like structure, which is associated with the uniform distribution of melanin on the dermal ridges and is characteristic of benign lesions. An atypical pigment network has an irregular structure and is more characteristic of malignant lesions. The identification of a negative pigment network is also used in the diagnosis of melanoma.

An atypical vascular pattern consists of irregularly distributed vessels of varying sizes and shapes, which are found in malignant lesions.

Branching refers to radiating (radial) growths extending from the pigmented lesion in various directions, which are found in malignant lesions.

A white-blue or gray-blue area with an irregular structure may be observed in malignant lesions.

Typical pigmentation: benign lesions exhibit uniform coloring in a single shade (brown or pink). Atypical pigmentation – in malignant lesions, an irregular distribution of different colors within a single lesion (light brown, dark brown, black, red, white, or blue-gray).

Isolated dots are found in benign lesions. Atypical dots (an irregularly distributed cluster of dots) are found in malignant lesions. Globules are round or oval structures located in the center or at the periphery of the lesion. Globules of uniform size and color with a regular distribution are found in benign lesions. Atypical globules (of varying size and color and with an irregular distribution) are found in malignant lesions.

Areas of regression are white scar-like depigmentation or blue-gray pepper-like areas that are irregularly distributed within the tumor.

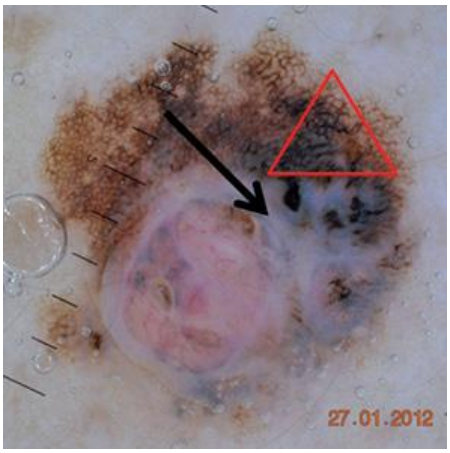

Fig. 3 Dermatoscopic image of melanoma (asymmetry of the pigmented lesion, atypical pigment network, white-blue areas)

The following statistical indicators of diagnostic algorithms are most commonly used:

1. Sensitivity is the ratio of the number of patients identified by the diagnostic algorithm to the true number of patients.
2. Specificity is the ratio of the number of healthy individuals identified by the diagnostic algorithm to the true number of healthy individuals.

The sensitivity of melanoma diagnosis using dermoscopy varies significantly; according to an analysis by an experienced dermoscopist, it has a sensitivity of 39% and a specificity of 82% [11], while other studies report higher sensitivity values of 68% [12, 13] and specificity values of 58% [14].

Table 2 presents statistical indicators for melanoma diagnostic methods.

Table 2

Statistical indicators for melanoma diagnostic methods

Diagnostic algorithm	Sensitivity	Specificity
ABCDE	92-97%	13-63%
Seven-sign	79-100%	30-37%

Conventional clinical diagnosis of skin lesions is characterized by a high degree of subjectivity in assessments and significant inter-expert variability, which stems from the limited accuracy of traditional diagnostic methods, particularly dermatoscopy and histopathology. The implementation of deep neural networks allows these limitations to be overcome, providing reliable and efficient classification of skin lesions, while transforming dermatological diagnosis into highly accurate automated systems for differentiating pathologies.

Currently, artificial neural networks are the most widely used machine learning methods for the intelligent diagnosis of melanoma [15-17]. They enable large-scale filtering of vast volumes of dermatoscopic images, gradually identifying diagnostically significant features: geometric characteristics of edges, textural anomalies, and chromatic variations. Their ability to automatically generate a high-dimensional feature space makes them a leading tool in the classification of skin pathologies.

Advantages of neural networks [15-17]:

– the ability to use a “black box” model, i.e., the structure and operating mechanism of the system are unknown, and only the input and output data are known;
– the ability to train and adapt them;
– parallel data processing (for non-recurrent neural networks).

Disadvantages of neural networks [15-17]:

– difficulty in generating training data;
– lack of a procedure for automatically determining the number of layers and neurons in each layer for specific tasks;
– high probability of the training method getting stuck in a local optimum;
– the knowledge generated by the neural network is incomprehensible to humans, as it is represented in the form of associative connections between neurons.

Currently, fuzzy expert systems are the most widely used among expert systems for the intelligent diagnosis of melanoma [18-22].

Advantages of fuzzy expert systems [18-22]:

– knowledge is represented as fuzzy rules that are understandable to humans;
– qualitative assessments of input and output data replace quantitative assessments;
– the procedure for obtaining knowledge from an expert is simplified.

Disadvantages of fuzzy expert systems [18-22]:

– inability to process information in parallel;
– the structure and parameters of membership functions used to describe input and output data cannot be automatically identified.

Recent studies indicate that modern methods of intelligent analysis demonstrate diagnostic accuracy comparable to that of experienced dermatologists in terms of the sensitivity and specificity of melanoma detection [23, 24].

Purpose, objectives and methods of research

Thus, the development of an intelligent melanoma diagnostic system that will eliminate these shortcomings is a pressing need, representing a new contribution to research on this issue.

The purpose of the study is to improve the effectiveness of melanoma diagnosis through digital image processing and a neuro-fuzzy expert system.

To achieve this goal, the following tasks must be addressed:

1. Calculation of melanoma features based on digital image processing.
2. Creation of a fuzzy expert system for melanoma diagnosis.
3. Selection of evaluation criteria for the effectiveness of the fuzzy expert system for melanoma diagnosis.
4. Conducting a numerical study.

1. Detection of melanoma features based on digital image processing

1.1. Conversion of a color image to a grayscale image

A color image (with components $R(n_1,n_2), G(n_1,n_2), B(n_1,n_2)$) is converted to a grayscale image (luminance) $g(n_1,n_2)$ as follows:

$$GS(n_1,n_2)=[R(n_1,n_2)\cdot 0.2125+G(n_1,n_2)\cdot 0.7154+B(n_1,n_2)\cdot 0.0721],$$

where $[]$ denotes the floor function.

A Gaussian filter [22] can be applied to the resulting grayscale image to remove noise.

1.2. Conversion of a grayscale image to a binary image based on single-level global thresholding with the Otsu threshold

Single-level global thresholding (global image binarization), which converts a grayscale image $GS(n_1,n_2)$ to a binary image $b(n_1,n_2)$, is expressed as

$$b(n_1,n_2)=\begin{cases}1, & GS(n_1,n_2)>T\\ 0, & GS(n_1,n_2)\le T\end{cases}.$$

The threshold T is determined based on the Otsu method as follows [25].

Let L is the number of brightness levels in the gray-scale image $GS(n_1,n_2)$, and n_k is the number of pixels with brightness k, $k\in\overline{0,L-1}$.

1. Calculation of histogram components

$$p_k=\frac{n_k}{N_1N_2},\ k\in\overline{0,L-1}.$$

2. Calculating first-order probability $P_1(k)$

$$P_1(k)=\sum_{i=0}^{k}p_i,\ k\in\overline{0,L-1}.$$

3. Calculating second-order probability $P_2(k)$

$$P_2(k)=1-P_1(k),\ k\in\overline{0,L-1}.$$

4. Calculating average brightness μ

$$\mu=\sum_{i=0}^{L}ip_i.$$

5. Calculation of the first-class expected value $\mu_1(k)$

$$\mu_1(k)=\frac{\sum_{i=0}^{k} ip_i}{P_1(k)},\ k\in\overline{0,L-1}.$$

6. Calculation of the second-class expected value $\mu_2(k)$

$$\mu_2(k)=\frac{\mu-\mu_1(k)P_1(k)}{P_2(k)},\ k\in\overline{0,L-1}.$$

7. Calculation of the interclass variance $\sigma^2(k)$

$$\sigma^2(k)=\frac{(\mu_1(k)-\mu_2(k))^2}{P_1(k)P_2(k)},\ k\in\overline{0,L-1}.$$

8. Calculation of the Otsu threshold

$$T=\arg\max_k \sigma^2(k),\ k\in\overline{0,L-1}.$$

1.3. Removal of small objects from a binary image using morphological transformation

The opening morphological operation is used to remove small objects from a binary image $b(n_1,n_2)$, which sequentially performs erosion and dilation operations [25].

Erosion can be defined as

$$\hat{b}(n_1,n_2)=\min_{(m_1,m_2)\in U_{(n_1,n_2)}}\{b(m_1,m_2)\},\ n_1\in\overline{M,N_1-M+1},\ n_2\in\overline{M,N_2-M+1},$$

where $U_{(n_1,n_2)}$ is the (square) Moore neighborhood of point (n_1,n_2).

Dilation can be defined as

$$\breve{b}(n_1,n_2)=\max_{(m_1,m_2)\in U_{(n_1,n_2)}}\{\hat{b}(m_1,m_2)\},\ n_1\in\overline{M,N_1-M+1},\ n_2\in\overline{M,N_2-M+1},$$

where $U_{(n_1,n_2)}$ is the (square) Moore neighborhood of point (n_1,n_2).

1.4. Generation of the binary membership matrix for image points and the grayscale image of the object

The binary membership matrix for image points $\bar{B}=[\bar{b}_{n_1,n_2}]$ is defined as the inverted binary image following morphological transformation $\breve{b}(n_1,n_2)$, i.e., $\bar{b}_{n_1,n_2}=1-\breve{b}(n_1,n_2)$.

The grayscale image $GS(n_1,n_2)$ is multiplied by the binary matrix of image point membership to the object $\bar{B}=[\bar{b}_{n_1,n_2}]$, resulting in the image $O(n_1,n_2)$, $n_1\in\overline{0,N_1-1}, n_2\in\overline{0,N_2-1}$, i.e., $O(n_1,n_2)=GS(n_1,n_2)\bar{b}_{n_1,n_2}$, $n_1\in\overline{0,N_1-1}, n_2\in\overline{0,N_2-1}$.

1.5. Determining the boundary of an object in a binary image after morphological transformation using the canny method

The Canny method is the best method for detecting brightness changes (or object boundaries) [25].

Let $\breve{b}(n_1,n_2)$, $n_1\in\overline{0,N_1-1}, n_2\in\overline{0,N_2-1}$ is the binary image after morphological transformation.

1. Noise removal using a Gaussian filter with normalization

$$\tilde{b}(n_1,n_2)=\sum_{m_1=-2}^{2}\sum_{m_2=-2}^{2}h(m_1,m_2)\breve{b}(n_1-m_1,n_2-m_2),$$

$$h(m_1,m_2)=\frac{\frac{1}{\sqrt{2\pi}\sigma}\exp\left(-\frac{1}{2}\frac{m_1^2+m_2^2}{\sigma^2}\right)}{\sum_{k=-M}^{M}\sum_{l=-M}^{M}\frac{1}{\sqrt{2\pi}\sigma}\exp\left(-\frac{1}{2}\frac{m_1^2+m_2^2}{\sigma^2}\right)}.$$

2. Gradient search

2.1. Calculation of the gradient magnitude

$$g(n_1,n_2)=\sum_{i=1}^{2}\left|\sum_{m_1=-1}^{1}\sum_{m_2=-1}^{1}h^{(i)}(m_1,m_2)\tilde{b}(n_1-m_1,n_2-m_2)\right| \text{ or}$$

$$g(n_1,n_2)=\sqrt{\sum_{i=1}^{2}\left(\sum_{m_1=-1}^{1}\sum_{m_2=-1}^{1}h^{(i)}(m_1,m_2)\tilde{b}(n_1-m_1,n_2-m_2)\right)^2}.$$

2.2. Calculation of the gradient angle

$$\theta=\arctan\left(\frac{\sum_{m_1=-1}^{1}\sum_{m_2=-1}^{1}h^{(2)}(m_1,m_2)\tilde{b}(n_1-m_1,n_2-m_2)}{\sum_{m_1=-1}^{1}\sum_{m_2=-1}^{1}h^{(1)}(m_1,m_2)\tilde{b}(n_1-m_1,n_2-m_2)}\right)\cdot\frac{180}{\pi}.$$

If $\sum_{m_1=-1}^{1}\sum_{m_2=-1}^{1}h^{(1)}(m_1,m_2)\tilde{b}(n_1-m_1,n_2-m_2)=0$, then $\theta=90$.

It is recommended to use the following transfer functions for $h^{(i)}$:

– Sobel filter

$$h^{(1)}=\frac{1}{4}\begin{bmatrix}-1&0&1\\-2&0&2\\-1&0&1\end{bmatrix},\ h^{(2)}=\frac{1}{4}\begin{bmatrix}-1&-2&-1\\0&0&0\\1&2&1\end{bmatrix};$$

– Prewitt (Pruitt) filter

$$h^{(1)}=\frac{1}{3}\begin{bmatrix}-1&0&1\\-1&0&1\\-1&0&1\end{bmatrix},\ h^{(2)}=\frac{1}{3}\begin{bmatrix}-1&-1&-1\\0&0&0\\1&1&1\end{bmatrix};$$

– Frey-Chen filter

$$h^{(1)}=\frac{1}{2+\sqrt{2}}\begin{bmatrix}-1&0&1\\-\sqrt{2}&0&\sqrt{2}\\-1&0&1\end{bmatrix},\ h^{(2)}=\frac{1}{2+\sqrt{2}}\begin{bmatrix}-1&-\sqrt{2}&-1\\0&0&0\\1&\sqrt{2}&1\end{bmatrix}.$$

3. Suppression of non-maxima

$e(n_1,n_2)=g(n_1,n_2)$,

if $(-22.5<\theta<0)\vee(0<\theta<22.5)$ and $g(n_1,n_2)<g(n_1,n_2+1)$, then $e(n_1,n_2)=0$,

if $(-180<\theta<-157.5)\vee(157.5<\theta<180)$ and $g(n_1,n_2)<g(n_1,n_2-1)$, then $e(n_1,n_2)=0$,

if $(67.5<\theta<112.5)$ and $g(n_1,n_2)<g(n_1-1,n_2)$, then $e(n_1,n_2)=0$,

if $(-112.5<\theta<-67.5)$ and $g(n_1,n_2)<g(n_1+1,n_2)$, then $e(n_1,n_2)=0$,

if $(22.5<\theta<67.5)$ and $g(n_1,n_2)<g(n_1-1,n_2+1)$, then $e(n_1,n_2)=0$,

if $(-157.5<\theta<-112.5)$ and $g(n_1,n_2)<g(n_1+1,n_2-1)$, then $e(n_1,n_2)=0$,

if $112.5<\theta\le157.5$ and $g(n_1,n_2)<g(n_1-1,n_2-1)$, then $e(n_1,n_2)=0$,

if $-22.5<\theta\le-67.5$ and $g(n_1,n_2)<g(n_1+1,n_2+1)$, then $e(n_1,n_2)=0$.

4. Thresholding

The binary matrix of image point membership to the object boundary $\bar{E}=[\bar{e}_{n_1,n_2}]$ is initialized to zero, $\bar{e}_{n_1,n_2}=0$,

if $e(n_1,n_2)>t_{\max}$, then point (n_1,n_2) is a boundary point, $\bar{e}_{n_1,n_2}=1$,

if $t_{\min} < e(n_1, n_2) < t_{\max}$ and there is a point (m_1, m_2) in the neighborhood of point (n_1, n_2) that is a boundary point, i.e., $(m_1, m_2) \in U_{(n_1,n_2)}$, then point (n_1, n_2) is also a boundary point $\bar{e}_{n_1,n_2} = 1$,

$$U_{(n_1,n_2)} = \{(n_1-1, n_2-1), (n_1-1, n_2), (n_1-1, n_2+1), (n_1, n_2-1), (n_1, n_2),$$
$$(n_1, n_2+1), (n_1+1, n_2-1), (n_1+1, n_2), (n_1+1, n_2+1)\}.$$

1.6. Calculating the irregularity of an object's boundary in a binary image after morphological transformation

In the simplest case, the irregularity of an object's boundary in a binary image after morphological transformation is calculated as [26]

$$I = \frac{P^2}{4\pi A},\ P = \sum_{n_1=0}^{N_1-1}\sum_{n_2=0}^{N_2-1} \bar{e}(n_1, n_2),\ A = \sum_{n_1=0}^{N_1-1}\sum_{n_2=0}^{N_2-1} \bar{b}_{n_1,n_2},$$

where P is the perimeter (number of pixels on the object's boundary), and A is the area of the object (number of pixels inside the object).

If $I > 1.8$, then this is a boundary irregularity.

A more complex variant involves calculating boundary irregularity based on fractal dimension [26].

1.7. Determining the number of colors based on clustering of a gray-scale image object

In this work, DBSCAN was chosen as the clustering method, as it is robust to noise and different cluster shapes.

1. Set the size of the Moore neighborhood of point D. Set the maximum distance ε. Set the matrix of point labels $M(n_1, n_2) = 0$, $n_1 \in \overline{0, N_1 - 1}$, $n_2 \in \overline{0, N_2 - 1}$. Set the counter for the number of clusters (colors) $c = 0$.
2. Set the row number of the image $n_1 = 0$.
3. Set the column number of the image $n_2 = 0$.
4. Determine the number of the current image point $i = n_1 N_2 + n_2$.
5. If the i-th point is already labeled, i.e., $M(n_1, n_2) \neq 0$, then proceed to step 20.
6. Determine the neighborhood of the i-th point

$$U_{i,\varepsilon} = \{e \,|\, |O(n_1, n_2) - O(l_1 + n_1, l_2 + n_2)| \le \varepsilon\},\ e = (l_1 + n_1)N_2 + l_2 + n_2,\ l_1, l_2 \in \{-1, 0, 1\}.$$

7. If not all neighbors of the i-th point fall within its neighborhood, i.e., $|U_{i,\varepsilon}| < D$, then mark the i-th point as a random outlier or noise, i.e., $M(n_1, n_2) = -1$, and proceed to step 20.
8. Increment the counter of the number of connected regions, i.e., $c = c + 1$.
9. Mark the i-th point as the c-th cluster, i.e., $M(n_1, n_2) = c$.
10. Create the set $S = U_{i,\varepsilon}$.
11. Extract the first element from the set S, i.e., $v = s_1$, and remove it from the set S, i.e., $S = S \setminus \{v\}$.
12. Determine the coordinates of the v-th point in the image

$$m_2 = v \bmod N_2,\ m_1 = \left[(v - m_2)/N_2\right],$$

where $\bmod$ denotes modulo division, and $[]$ denotes the integer part of a number.

13. If the v-th point was marked as an outlier or noise, i.e., $M(m_1, m_2) = -1$, then mark it as the c-th cluster, i.e., $M(m_1, m_2) = c$.
14. If the v-th point is already marked, i.e., $M(m_1, m_2) \neq 0$, then proceed to step 19.
15. Mark the v-th point, i.e., $M(m_1, m_2) = c$.
16. Define the neighborhood of the v-th point

$$U_{v,\varepsilon} = \{e \,|\, |O(m_1, m_2) - O(l_1 + m_1, l_2 + m_2)| \le \varepsilon\},\ e = (l_1 + m_1)N_2 + l_2 + m_2,\ l_1, l_2 \in \{-1, 0, 1\}.$$

17. If not all neighbors of the v-th point fall within its neighborhood, i.e., $|U_{v,\varepsilon}| < D$, then proceed to step 19.

18. Merge the set S with the neighborhood of the v-th point, i.e., $S = S \bigcup U_{v,\varepsilon}$.

19. If the set S is non-empty, i.e., $|S| > 0$, then proceed to step 11.

20. If it is not the end of the current row of the image, i.e., $n_2 < N_2 - 1$, then increment the column number of the current row, i.e., $n_2 = n_2 + 1$, and proceed to step 4.

21. If it is not the last row of the image, i.e., $n_1 < N_1 - 1$, then increase the row number, i.e., $n_1 = n_1 + 1$, and proceed to step 3.

The result is the number of clusters (colors) c.

1.8. Rotation of the object in the gray-scale image

To calculate the diameter and check for asymmetry of the object, it is necessary to first rotate the object [27]. To rotate the object in the gray-scale image $Q(n_1, n_2)$, it is necessary to know the point about which the rotation is performed and the angle of rotation. To do this, we first calculate the following quantities.

The area of the image object is calculated as

$$S = \sum_{n_1=0}^{N_1-1} \sum_{n_2=0}^{N_2-1} \bar{b}_{n_1,n_2},$$

where $\bar{B} = [\bar{b}_{n_1,n_2}]$ is the binary matrix indicating which image points belong to the object.

The point with coordinates (x_c, y_c), about which the rotation is performed, is calculated as the center of mass of the image object as

$$x_c = \frac{1}{S} \sum_{n_1=0}^{N_1-1} \sum_{n_2=0}^{N_2-1} n_1 \bar{b}_{n_1,n_2}, \; y_c = \frac{1}{S} \sum_{n_1=0}^{N_1-1} \sum_{n_2=0}^{N_2-1} n_2 \bar{b}_{n_1,n_2}.$$

The second-order moments m_x, m_y, m_{xy} for the image object are calculated as

$$m_x = \frac{1}{S} \sum_{n_1=0}^{N_1-1} \sum_{n_2=0}^{N_2-1} (n_1 - x_c)^2 \bar{b}_{n_1,n_2}, \; m_y = \frac{1}{S} \sum_{n_1=0}^{N_1-1} \sum_{n_2=0}^{N_2-1} (n_2 - y_c)^2 \bar{b}_{n_1,n_2},$$

$$m_{xy} = \frac{1}{S} \sum_{n_1=0}^{N_1-1} \sum_{n_2=0}^{N_2-1} (n_1 - x_c)(n_2 - y_c) \bar{b}_{n_1,n_2}.$$

The rotation angle β (in radians) is calculated as the direction of the principal axis for the gray-scale image object based on the following equation

$$\tan 2\beta = \frac{2m_{xy}}{m_x - m_y}.$$

In the discrete case, the rotation of the gray-scale image object $O(n_1, n_2)$, which maps each point (n_1, n_2) to point (m_1, m_2), and the resulting rotated gray-scale image object $O^{turn}(m_1, m_2)$ is given by [27]

$$m_1 = [x_c + (n_1 - x_c) \cdot \cos\beta \mp (n_2 - y_c) \cdot \sin\beta], \; m_2 = [y_c \pm (n_1 - x_c) \cdot \sin\beta + (n_2 - y_c) \cdot \cos\beta].$$

where $[]$ denotes floor division.

The specific signs in rotation formulas depend on whether the coordinate system is right-handed or left-handed, and whether the rotation is clockwise or counterclockwise. The upper sign corresponds to a right-handed coordinate system and a positive counterclockwise rotation direction (or a left-handed coordinate system and a positive clockwise rotation direction), while the lower sign corresponds to the remaining two combinations.

A binary matrix is determined that indicates which image points belong to the rotated object $\bar{B}^{turn} = [\bar{b}^{turn}_{n_1,n_2}]$, i.e. $\bar{b}^{turn}_{n_1,n_2} = \begin{cases} 1, & O^{turn}(n_1, n_2) > 0 \\ 0, & O^{turn}(n_1, n_2) = 0 \end{cases}$.

1.9. Calculating the diameter of the rotated object in the grayscale image

The radius of the object is calculated as the distance from the center of the object to its farthest point

$$R = \max_{(n_1,n_2)} \sqrt{(n_1 - x_c)^2 \bar{b}^{turn}_{n_1,n_2} + (n_2 - y_c)^2 \bar{b}^{turn}_{n_1,n_2}}, \; n_1 \in \overline{0, N_1 - 1}, n_2 \in \overline{0, N_2 - 1}.$$

The diameter of the object is calculated

$$D = 2R.$$

1.10. Asymmetry check based on a rotated object in a gray-scale image

To check for asymmetry, the rotated object must first be split [27].

The rotated object in the grayscale image is split horizontally in half to obtain two images: one containing the upper half of the object, i.e., $O^{top}(n_1,n_2)$, $O^{top}(n_1,n_2) = \begin{cases} O^{turn}(n_1,n_2), & n_2 < N_2/2 \\ 0, & n_2 \geq N_2/2 \end{cases}$, and the other containing the lower half of the object, followed by a mirror reflection of the lower half of the object with respect to the horizontal axis, i.e., $O^{bottom}(n_1,n_2)$, $O^{bottom}(n_1,n_2) = \begin{cases} O^{turn}(n_1, N_2 - n_2), & n_2 < N_2/2 \\ 0, & n_2 \geq N_2/2 \end{cases}$.

Next, a binary matrix of points belonging to the upper half of the rotated object in the gray-scale image $\bar{B}^{top} = [\bar{b}^{top}_{n_1,n_2}]$, $\bar{b}^{top}_{n_1,n_2} = \begin{cases} \bar{b}^{turn}_{n_1,n_2}, & n_2 < N_2/2 \\ 0, & n_2 \geq N_2/2 \end{cases}$, and a binary matrix of points belonging to the mirror-reflected lower half of the rotated object in the gray-scale image $\bar{B}^{bottom} = [\bar{b}^{bottom}_{n_1,n_2}]$, $\bar{b}^{bottom}_{n_1,n_2} = \begin{cases} \bar{b}^{turn}_{n_1,N_2-n_2}, & n_2 < N_2/2 \\ 0, & n_2 \geq N_2/2 \end{cases}$, are computed.

The rotated object in the gray-scale image is split vertically in half to obtain two images containing the left half of the object, i.e., $O^{left}(n_1,n_2)$, $O^{left}(n_1,n_2) = \begin{cases} O^{turn}(n_1,n_2), & n_1 < N_1/2 \\ 0, & n_1 \geq N_1/2 \end{cases}$, and the right half of the object, followed by a vertical mirroring of the right half of the object, i.e., $O^{right}(n_1,n_2)$, $O^{right}(n_1,n_2) = \begin{cases} O^{turn}(N_1 - n_1, n_2), & n_1 < N_1/2 \\ 0, & n_1 \geq N_1/2 \end{cases}$.

Then, a binary matrix of points belonging to the left half of the rotated object in the gray-scale image $\bar{B}^{left} = [\bar{b}^{left}_{n_1,n_2}]$, $\bar{b}^{left}_{n_1,n_2} = \begin{cases} \bar{b}^{turn}_{n_1,n_2}, & n_1 < N_1/2 \\ 0, & n_1 \geq N_1/2 \end{cases}$, and a binary matrix of points belonging to the mirror-reflected right half of the rotated object in the gray-scale image $\bar{B}^{right} = [\bar{b}^{right}_{n_1,n_2}]$, $\bar{b}^{right}_{n_1,n_2} = \begin{cases} \bar{b}^{turn}_{N_1-n_1,n_2}, & n_1 < N_1/2 \\ 0, & n_1 \geq N_1/2 \end{cases}$, are computed.

The area of the rotated image object is calculated as

$$S^{turn} = \sum_{n_1=0}^{N_1-1} \sum_{n_2=0}^{N_2-1} \bar{b}^{turn}_{n_1,n_2},$$

where $\bar{B}^{turn} = [\bar{b}^{turn}_{n_1,n_2}]$ is a binary matrix indicating which image points belong to the rotated object.

The brightness asymmetry of the object with respect to the horizontal axis is calculated as [27]

$$a^{bh} = \frac{1}{S^{turn}} \sum_{n_1=0}^{N_1-1} \sum_{n_2=0}^{N_2-1} \left| O^{top}(n_1,n_2) - O^{bottom}(n_1,n_2) \right|.$$

The brightness of the object relative to the horizontal axis is asymmetric if $a^{bh} > 0.03$.

The brightness asymmetry of the object relative to the vertical axis is calculated as [27]

$$a^{bv} = \frac{1}{S^{turn}} \sum_{n_1=0}^{N_1-1} \sum_{n_2=0}^{N_2-1} \left| O^{left}(n_1, n_2) - O^{right}(n_1, n_2) \right|.$$

The brightness of the object relative to the vertical axis is asymmetric if $a^{bv} > 0.03$.
The shape asymmetry of the object relative to the horizontal axis is calculated as [27]

$$a^{sh} = \frac{1}{S^{turn}} \sum_{n_1=0}^{N_1-1} \sum_{n_2=0}^{N_2-1} \left| \bar{b}^{top}_{n_1,n_2} - \bar{b}^{bottom}_{n_1,n_2} \right|.$$

The shape of the object for the horizontal axis is asymmetric if $a^{sh} > 0.02$.
The asymmetry of the object's shape for the vertical axis is calculated as [27]

$$a^{sv} = \frac{1}{S^{turn}} \sum_{n_1=0}^{N_1-1} \sum_{n_2=0}^{N_2-1} \left| \bar{b}^{left}_{n_1,n_2} - \bar{b}^{right}_{n_1,n_2} \right|.$$

The shape of the object for the vertical axis is asymmetric if $a^{sv} > 0.02$.

2. Development of a fuzzy expert system for melanoma diagnosis

For the diagnosis of melanoma, this study further refined a fuzzy expert system that utilizes Sugeno's fuzzy inference algorithm and involves the following steps:

- formulation of linguistic variables;
- formulation of a fuzzy rule base;
- fuzzification;
- aggregation of subconditions;
- activation of conclusions;
- defuzzification.

2.1. Formation of linguistic variables

The following were selected as crisp input variables:

- the degree of border irregularity x_1;
- the number of colors x_2;
- the diameter x_3;
- the brightness asymmetry value for the horizontal axis x_4;
- the brightness asymmetry value for the vertical axis x_5;
- the shape asymmetry value for the horizontal axis x_6;
- the shape asymmetry value for the vertical axis x_7.

The following were selected as linguistic input variables:

- boundary irregularity $\tilde{x}_1$ with its values $\tilde{\alpha}_{11} = \text{low}, \tilde{\alpha}_{12} = \text{medium}, \tilde{\alpha}_{13} = \text{high}$, where the value ranges are fuzzy sets $\tilde{A}_{11} = \{x_1 \mid \mu_{\tilde{A}_{11}}(x_1)\}$, $\tilde{A}_{12} = \{x_1 \mid \mu_{\tilde{A}_{12}}(x_1)\}$, $\tilde{A}_{13} = \{x_1 \mid \mu_{\tilde{A}_{13}}(x_1)\}$;
- number of colors $\tilde{x}_2$ with its values $\tilde{\alpha}_{21} = \text{low}, \tilde{\alpha}_{22} = \text{medium}, \tilde{\alpha}_{23} = \text{high}$, where the value ranges are fuzzy sets $\tilde{A}_{21} = \{x_2 \mid \mu_{\tilde{A}_{21}}(x_2)\}$, $\tilde{A}_{22} = \{x_2 \mid \mu_{\tilde{A}_{22}}(x_2)\}$, $\tilde{A}_{23} = \{x_2 \mid \mu_{\tilde{A}_{23}}(x_2)\}$;
- diameter $\tilde{x}_3$ with its values $\tilde{\alpha}_{31} = \text{low}, \tilde{\alpha}_{32} = \text{medium}, \tilde{\alpha}_{33} = \text{high}$, where the value ranges are fuzzy sets $\tilde{A}_{31} = \{x_3 \mid \mu_{\tilde{A}_{31}}(x_3)\}$, $\tilde{A}_{32} = \{x_3 \mid \mu_{\tilde{A}_{32}}(x_3)\}$, $\tilde{A}_{33} = \{x_3 \mid \mu_{\tilde{A}_{33}}(x_3)\}$;
- brightness asymmetry for the horizontal axis $\tilde{x}_4$ with its values $\tilde{\alpha}_{41} = \text{low}, \tilde{\alpha}_{42} = \text{medium}, \tilde{\alpha}_{43} = \text{high}$, where the domains are fuzzy sets $\tilde{A}_{41} = \{x_4 \mid \mu_{\tilde{A}_{41}}(x_4)\}$, $\tilde{A}_{42} = \{x_4 \mid \mu_{\tilde{A}_{42}}(x_4)\}$, $\tilde{A}_{43} = \{x_4 \mid \mu_{\tilde{A}_{43}}(x_4)\}$;

– brightness asymmetry $\tilde{x}_5$ for the vertical axis with its values $\tilde{\alpha}_{51} = \text{low}, \tilde{\alpha}_{52} = \text{medium}, \tilde{\alpha}_{53} = \text{high}$, where the domains are fuzzy sets $\tilde{A}_{51} = \{x_5 \mid \mu_{\tilde{A}_{51}}(x_5)\}$, $\tilde{A}_{52} = \{x_5 \mid \mu_{\tilde{A}_{52}}(x_5)\}$, $\tilde{A}_{53} = \{x_5 \mid \mu_{\tilde{A}_{53}}(x_5)\}$;

– shape asymmetry $\tilde{x}_6$ for the horizontal axis with its values $\tilde{\alpha}_{61} = low, \tilde{\alpha}_{62} = medium, \tilde{\alpha}_{63} = high$, where the value ranges are fuzzy sets $\tilde{A}_{61} = \{x_6 \mid \mu_{\tilde{A}_{61}}(x_6)\}$, $\tilde{A}_{62} = \{x_6 \mid \mu_{\tilde{A}_{62}}(x_6)\}$, $\tilde{A}_{63} = \{x_6 \mid \mu_{\tilde{A}_{63}}(x_6)\}$.

– shape asymmetry $\tilde{x}_7$ for the vertical axis with its values $\tilde{\alpha}_{71} = low, \tilde{\alpha}_{72} = medium, \tilde{\alpha}_{73} = high$, where the value ranges are fuzzy sets $\tilde{A}_{71} = \{x_7 \mid \mu_{\tilde{A}_{71}}(x_7)\}$, $\tilde{A}_{72} = \{x_7 \mid \mu_{\tilde{A}_{72}}(x_7)\}$, $\tilde{A}_{73} = \{x_7 \mid \mu_{\tilde{A}_{73}}(x_7)\}$.

The state number of the formation y (1 is benign, 2 is suspicious, 3 is malignant) was chosen as the crisp output variable.

2.2. Formulation of the fuzzy rule base

The proposed fuzzy rules account for all possible combinations of values for the input linguistic variables and the corresponding values of the output linguistic variable:

For example, the fuzzy rule R^1 with weight F^1 corresponds to the following knowledge: if the boundary irregularity is small and the diameter is small and the number of colors is small and the brightness asymmetry is small and the shape asymmetry is small, then the formation is benign ($y = 1$).

R^1: IF $\tilde{x}_1$ there is $\tilde{\alpha}_{11}$ AND $\tilde{x}_2$ there is $\tilde{\alpha}_{21}$ AND $\tilde{x}_3$ there is $\tilde{\alpha}_{31}$ AND $\tilde{x}_4$ there is $\tilde{\alpha}_{41}$ AND $\tilde{x}_5$ there is $\tilde{\alpha}_{51}$ AND $\tilde{x}_6$ there is $\tilde{\alpha}_{61}$ AND $\tilde{x}_7$ there is $\tilde{\alpha}_{71}$ THEN $y = \varepsilon_0^1 + \sum_{i=1}^{7} \varepsilon_i^1 x_i$ (F^1),

where ε_i^k is given weight coefficients.

2.3. Fuzzification

Let us define the degree of truth of each subcondition of each fuzzy rule using the membership function $\mu_{\tilde{A}_{ij}}(x_i)$.

The membership functions of the subcondition $\tilde{x}_i$ is $\tilde{\alpha}_{i1}$ are defined as

$$\mu_{\tilde{A}_{i1}}(x_i) = \frac{1}{1 + \exp(a_{i1}(x_i - b_{i1}))}, \; a_{i1} > 0.$$

The membership functions of the subcondition $\tilde{x}_i$ is $\tilde{\alpha}_{i2}$ are defined as

$$\mu_{\tilde{A}_{i2}}(x_i) = \exp\left(-\left|\frac{x - b_{i2}}{a_{i2}}\right|^{c_{i2}}\right), \; a_{i2} > 0, \; c_{i2} > 0.$$

The membership functions of the subcondition $\tilde{x}_i$ is $\tilde{\alpha}_{i3}$ are defined as

$$\mu_{\tilde{A}_{i3}}(x_i) = \frac{1}{1 + \exp(-a_{i3}(x_i - b_{i3}))}, \; a_{i3} > 0.$$

where a_{ij}, b_{ij}, and c_{ij} are parameters.

2.4. Aggregation of subconditions

Let us define the truth value of each condition of each fuzzy rule as

$$a2^k = \prod_{i=1}^{7} \mu_{\tilde{A}_{ij_k}}(x_i), \; j_k \in \overline{1,3}, \; k \in \overline{1,r}.$$

2.5. Activation of conclusions

First, the truth values of the conditions of the fuzzy rules are multiplied by their weights

$a3^k = a2^k F^k$, $k \in \overline{1,r}$.

In this work, the weight coefficients of the fuzzy rules F^r are defined as

$F^r = 1.$

Next, the conclusions are calculated, which involves determining the values of the output crisp variables for each fuzzy production using the weighted sum method

$$z^k = \varepsilon_0^k + \sum_{i=1}^{7} \varepsilon_i^k x_i, \; k \in \overline{1,r}.$$

2.6. Defuzzification

To obtain the state number of the formation, the weighted sum method is used

$$y = \sum_{k=1}^{r} a3^k z^k .$$

3. Selection of evaluation criteria for the performance of a fuzzy expert system for melanoma diagnosis

In this study, the following criteria were selected to evaluate the performance of a fuzzy expert system for melanoma diagnosis:

– the accuracy criterion, which involves selecting parameter values $\theta = (a_{11}, b_{11}, a_{12}, b_{12}, c_{12}, a_{13}, b_{13}, ..., a_{71}, b_{71}, a_{72}, b_{72}, c_{72}, a_{73}, b_{73})$ that minimize the mean squared error (the difference between the fuzzy expert system's output and the test output)

$$F = \frac{1}{3P} \sum_{p=1}^{P} \sum_{z=1}^{3} (y_{pz} - d_{pz})^2 \to \min_{\theta} \quad (1)$$

where d_{pz} is the test output, $d_{pz} \in \{0,1\}$, y_{pz} is the output of the fuzzy expert system, and P is the number of test runs.

– the reliability criterion, which involves selecting parameter values $\theta = (a_{11}, b_{11}, a_{12}, b_{12}, c_{12}, a_{13}, b_{13}, ..., a_{71}, b_{71}, a_{72}, b_{72}, c_{72}, a_{73}, b_{73})$ that minimize the probability of an incorrect decision (the difference between the output of the fuzzy expert system and the test output)

$$F = \frac{1}{P} \sum_{p=1}^{P} \left[\arg\max_{z \in 1,3} y_{pz} \neq \arg\max_{z \in 1,3} d_{pz} \right] \to \min_{\theta}, \quad (2)$$

$$\left[\arg\max_{z \in 1,3} y_z \neq \arg\max_{z \in 1,3} d_{pz} \right] = \begin{cases} 1, & \arg\max_{z \in 1,3} y_z \neq \arg\max_{z \in 1,3} d_{pz} \\ 0, & \arg\max_{z \in 1,3} y_z = \arg\max_{z \in 1,3} d_{pz} \end{cases}.$$

– the speed criterion, which means selecting such values of the parameters $\theta = (a_{11}, b_{11}, a_{12}, b_{12}, c_{12}, a_{13}, b_{13}, ..., a_{71}, b_{71}, a_{72}, b_{72}, c_{72}, a_{73}, b_{73})$ that minimize computational complexity

$$F = T \to \min_{\theta}. \quad (3)$$

Experiments

A numerical analysis of the proposed fuzzy expert system was conducted using Python.

Table 1 presents the computational complexity, root mean square errors (RMSE), and probabilities of incorrect decisions in melanoma diagnosis obtained on the Melanoma Detection Dataset [28], which contains RGB images of size 4288 x 2848, where 1,746 images were randomly selected from 2,364 images for the training set, and 618 images were selected for the validation set (108 images) and the test set (510 images), where P is the number of test runs, $W\ 1$ is the number of parameters of the CNN neural network, and $W\ 2$ is the number of parameters of the fuzzy expert system.

Table 3

Computational complexity, mean squared error, and probability of incorrect decisions in melanoma diagnosis

Model and parameter identification method	RMSE	Probability of making an incorrect decision	Computational complexity
CNN neural network	0.10	0.05	$T = PW\ 1$
Fuzzy expert system	0.05	0.02	$T = PW\ 2$

According to Table 3, the fuzzy expert system yields the best results.

Conclusions

1. To address the challenge of improving the accuracy of melanoma diagnosis, relevant artificial intelligence methods were investigated. These studies have shown that, to date, the most effective approach is the use of a fuzzy expert system with preliminary digital signal processing.
2. The novelty of this study lies in the fact that the proposed fuzzy expert system represents knowledge about melanoma in the form of fuzzy rules that are understandable to humans; it reduces computational complexity, the probability of making an incorrect decision, and the mean squared error.
3. As a result of numerical analysis, it was established that the proposed fuzzy expert system yields a probability of incorrect decisions in melanoma diagnosis of 0.02 and a root mean square error of 0.05.
4. Future research prospects include the use of the proposed fuzzy expert system in various intelligent decision support systems.

ADDITIONAL INFORMATION

AUTHOR CONTRIBUTIONS

Conceptualization, E.F.; methodology, T.U.; validation, Y.K.; formal analysis, T.U.; investigation, Y.K.; data curation, E.F.; writing-original draft preparation, T.U.; writing-review and editing, E.F.; visualization, Y.K.; supervision, T.U.; project administration, E.F. All authors have read and agreed to the published version of the manuscript.

DECLARATION ON THE USE OF GENERATIVE ARTIFICIAL INTELLIGENCE TOOLS

In preparing this work, the author used DeepL Translate and Grammarly for: grammar and spelling checks, paraphrasing, and rephrasing. After using these tools/services, the author reviewed and edited the content and takes full responsibility for the content of this publication.

1. MacKie R. M., Hauschild A., Eggermont A. M. Epidemiology of Invasive Cutaneous Melanoma. *Annals of Oncology*. 2009. Vol. 20, Suppl. 6. P. 1-7. DOI: https://doi.org/10.1093/annonc/mdp252.
2. Meyle K. D., Guldberg P. Genetic Risk Factors for Melanoma. *Human Genetics*. 2009. Vol. 126, No. 4. P. 499-510. DOI: https://doi.org/10.1007/s00439-009-0715-9.
3. Cancer Today : online platform / International Agency for Research on Cancer. URL: https://gco.iarc.who.int/today/en/dataviz/maps-heatmap?mode=population&cancers=16.
4. Mistry M., Parkin D. M., Ahmad A. S., Sasieni P. Cancer Incidence in the United Kingdom: Projections to the Year 2030. *British Journal of Cancer*. 2011. Vol. 105, No. 11. P. 1795-1803. DOI: https://doi.org/10.1038/bjc.2011.430.
5. Wang M., Gao X., Zhang L. Recent Global Patterns in Skin Cancer Incidence, Mortality, and Prevalence. *Chinese Medical Journal*. 2025. Vol. 138, No. 2. P. 185-192. DOI: https://doi.org/10.1097/CM9.0000000000003416.
6. Analysis of Global Skin Cancer Epidemiology in 2022 and Correlation with Dermatologist Density / S. Salah, D. Kerob, K. Ezzedine et al. Journal of the European Academy of Dermatology and Venereology. 2026. Vol. 40, Issue 1. P. e221-e223. DOI: https://doi.org/10.1111/jdv.20883.
7. Darweesh H. A., Najeeb S. J. An In-Depth Review of Leveraging Deep Learning Advancements for Enhanced Skin Cancer Detection and Classification. *Dasinya Journal for Engineering and Informatics*. 2026. Vol. 2, No. 1. DOI: https://doi.org/10.65542/djei.v2i1.26.
8. Semiological Value of ABCDE Criteria in the Diagnosis of Cutaneous Pigmented Tumors / L. Thomas et al. *Dermatology*. 1998. Vol. 197, No. 1. P. 11-17. DOI: https://doi.org/10.1159/000017969.
9. Okuboyejo D. A., Olugbara O. O. A Review of Prevalent Methods for Automatic Skin Lesion Diagnosis. *The Open Dermatology Journal*. 2018. Vol. 12. P. 14-53. DOI: https://doi.org/10.2174/1874372201812010014.
10. An Evaluation of the Revised Seven-Point Checklist for the Early Diagnosis of Cutaneous Melanoma / M. F. Healsmith et al. *British Journal of Dermatology*. 1994. Vol. 130, No. 1. P. 48-50. DOI: https://doi.org/10.1111/j.1365-2133.1994.tb06881.x.
11. The Diagnostic Performance of Expert Dermoscopists vs a Computer-Vision System on Small-Diameter Melanomas / R. J. Friedman et al. *Archives of Dermatology*. 2008. Vol. 144, No. 4. P. 476-482. DOI: https://doi.org/10.1001/archderm.144.4.476.
12. Diagnostic Accuracy of Dermoscopy / H. Kittler et al. *The Lancet Oncology*. 2002. Vol. 3, No. 3. P. 159-165. DOI: https://doi.org/10.1016/s1470-2045(02)00679-4.
13. Epiluminescence Microscopy. A Useful Tool for the Diagnosis of Pigmented Skin Lesions for Formally Trained Dermatologists / M. Binder et al. *Archives of Dermatology*. 1995. Vol. 131, No. 3.

P. 286-291. DOI: https://doi.org/10.1001/archderm.131.3.286.

14. Westerhoff K., McCarthy W. H., Menzies S. W. Increase in the Sensitivity for Melanoma Diagnosis by Primary Care Physicians using Skin Surface Microscopy. *British Journal of Dermatology*. 2000. Vol. 143, No. 5. P. 1016-1020. DOI: https://doi.org/10.1046/j.1365-2133.2000.03836.x.

15. Sivanandam S. N., Sumathi S., Deepa S. N. Introduction to Neural Networks using Matlab 6.0. New Delhi : The McGraw-Hill Comp., Inc., 2006. 660 p. URL: https://api.semanticscholar.org/CorpusID:60273182.

16. Haykin S. Neural Networks and Learning Machines. 3rd ed. Upper Saddle River, New Jersey : Pearson Education, Inc., 2009. 906 p. URL: https://dai.fmph.uniba.sk/courses/NN/haykin.neural-networks.3ed.2009.pdf.

17. Du K.-L., Swamy K. M. S. Neural Networks and Statistical Learning. London : Springer-Verlag, 2014. 824 p. DOI: https://doi.org/10.1007/978-1-4471-5571-3.

18. Egg Fertility Detection Using Image Processing and Fuzzy Logic / J. G. C. Rancapan et al. *International Journal of Scientific & Technology Research*. 2019. Vol. 8, Issue 10. P. 3228-3230. URL: https://www.ijstr.org/final-print/oct2019/Egg-Fertility-Detection-Using-Image-Processing-And-Fuzzy-Logic.pdf.

19. Fuzzy Logics Associated with Neural Networks in The Real Time for Better World / G. P. Reddy et al. *Proceedings of the International Conference on Advancements in Aeromechanical Materials for Manufacturing (ICAAMM-2016)*. 2017. P. 8507-8516. URL: https://api.semanticscholar.org/CorpusID:67869758.

20. Yen V. T., Wang Y. N., Cuong P. V. Recurrent Fuzzy Wavelet Neural Networks Based on Robust Adaptive Sliding Mode Control for Industrial Robot Manipulators. *Neural Computing and Applications*. 2019. Vol. 31, No. 11. P. 6925-6958. URL: https://api.semanticscholar.org/CorpusID:21695731.

21. Das H., Naik B., Behera H. S. Medical Disease Analysis using Neuro-Fuzzy with Feature Extraction Model for Classification. *Informatics in Medicine Unlocked*. 2020. Vol. 18. Art. 100288. DOI: https://doi.org/10.1016/j.imu.2020.100288.

22. Identification of Melanoma from Nevus Images / S. Bharathi et al. *Journal of Physics: Conference Series*. 2021. Vol. 1917. Art. 012027. DOI: https://doi.org/10.1088/1742-6596/1917/1/012027.

23. Artificial Intelligence Performance in Image-Based Cancer Identification: Umbrella Review of Systematic Reviews / H. L. Xu, T. T. Gong, X. J. Song et al. *Journal of Medical Internet Research*. 2025. Vol. 27. Art. e53567. DOI: https://doi.org/10.2196/53567.

24. Performance of Commercial Dermatoscopic Systems that Incorporate Artificial Intelligence for the Identification of Melanoma in General Practice: A Systematic Review / I. Miller, N. Rosic, M. Stapelberg et al. *Cancers*. 2024. Vol. 16, No. 7. Art. 1443. DOI: https://doi.org/10.3390/cancers16071443.

25. Ashafuddula N. I. Md., Islam R. Melanoma Skin Cancer and Nevus Mole Classification using Intensity Value Estimation with Convolutional Neural Network. *Computer Science*. 2023. Vol. 24, No. 3. P. 277-296. DOI: https://doi.org/10.7494/csci.2023.24.3.4844.

26. Ali A.-R., Li J., Yang G., O'Shea S. J. A Machine Learning Approach to Automatic Detection of Irregularity in Skin Lesion Border using Dermoscopic Images. *PeerJ Computer Science*. 2020. Vol. 6. Art. e268. DOI: https://doi.org/10.7717/peerj-cs.268.

27. Chatterjee S., Dey D., Munshi S., Gorai S. Dermatological Expert System Implementing the ABCD Rule of Dermoscopy for Skin Disease Identification. *Expert Systems with Applications*. 2021. Vol. 167. Art. 114204. DOI: https://doi.org/10.1016/j.eswa.2020.114204.

28. Gallo Henrique. Skin Cancer Melanoma CNN Transfer Learning. *Kaggle*. URL: https://www.kaggle.com/code/gallo33henrique/skin-cancer-melanoma-cnn-transfer-learning.

Євген ФЕДОРОВ, Тетяна УТКІНА, Ярослав КОРПАНЬ
Черкаський державний технологічний університет

МЕТОДИ ДІАГНОСТИКИ МЕЛАНОМИ НА ОСНОВІ ЦИФРОВОЇ ОБРОБКИ ЗОБРАЖЕНЬ ТА ЕКСПЕРТНИХ СИСТЕМ

У статті запропоновано рішення актуальної науково-прикладної задачі щодо створення методу діагностики меланоми на основі нечіткої експертної системи та цифрової обробки зображень. Запропонований у статті розрахунок ознак меланоми на основі цифрової обробки зображення включає в себе: перетворення кольорового зображення у сіре зображення; перетворення сірого зображення у бінарне на основі однорівневої глобальної порогової обробки з порогом Оцу; видалення дрібних об'єктів бінарного зображення за допомогою морфологічного перетворення; формування бінарної матриці приналежності точок зображення до об'єкта та сірого зображення об'єкта; визначення межі об'єкта бінарного зображення після морфологічного перетворення на основі методу Канні; обчислення нерегулярності межі об'єкта бінарного зображення після морфологічного перетворення; визначення кількості кольорів на основі кластеризації об'єкта сірого зображення; поворот об'єкта сірого зображення; обчислення діаметра повернутого об'єкта сірого зображення; перевірку асиметрії на основі

повернутого об'єкта сірого зображення. Для діагностики меланом у роботі було вдосконалено нечітку експертну систему діагностики меланоми, яка використовує алгоритм нечіткого виведення Сугено. Експериментальне дослідження підтвердило, що запропонована нечітка експертна система забезпечує ймовірність прийняття неправильних рішень щодо діагностики меланоми на рівні 0,02, а середньоквадратичну похибку – 0,05. Наукова новизна дослідження полягає в тому, що запропонована нечітка експертна система забезпечує представлення знань про меланому у вигляді нечітких правил, доступних для розуміння людиною; зменшує обчислювальну складність, ймовірність прийняття неправильного рішення та середньоквадратичну похибку. Запропоноване рішення є масштабованим і придатним для застосування в інтелектуальних системах прийняття рішень.

Ключові слова: нечітка експертна система діагностики меланоми, бінаризація зображення, геометричні перетворення зображення, кластеризація зображення, визначення меж об'єктів зображення, морфологічне перетворення зображення.